Hindawi
Advances in Materials Science and Engineering
Volume 2019, Article ID 2812748, 16 pages
https://doi.org/10.1155/2019/2812748

Research Article

A Coupling Electromechanical Inhomogeneous Cell-Based Smoothed Finite Element Method for Dynamic Analysis of Functionally Graded Piezoelectric Beams

Bin Cai [1] **and Liming Zhou** [2]

[1]*School of Civil Engineering, Jilin Jianzhu University, Changchun, Jilin, China*
[2]*School of Mechanical and Aerospace Engineering, Jilin University, Changchun, Jilin, China*

Correspondence should be addressed to Bin Cai; bincai666@163.com

Received 16 April 2019; Accepted 7 July 2019; Published 6 August 2019

Guest Editor: Ayman E. Hamada

To accurately simulate the continuous property change of functionally graded piezoelectric materials (FGPMs) and overcome the overstiffness of the finite element method (FEM), we present an electromechanical inhomogeneous cell-based smoothed FEM (ISFEM) of FGPMs. Firstly, ISFEM formulations were derived to calculate the transient response of FGPMs, and then, a modified Wilson-θ method was deduced to solve the integration of the FGPM system. The true parameters at the Gaussian integration point in FGPMs were adopted directly to replace the homogenization parameters in an element. ISFEM provides a close-to-exact stiffness of the continuous system, which could automatically and more easily generate for complicated domains and thus significantly decrease numerical errors. The accuracy and trustworthiness of ISFEM were verified as higher than the standard FEM by several numerical examples.

1. Introduction

Because of their outstanding electromechanical properties, easy fabricability, and preparation flexibility, piezoelectric materials are extensively applied as sensors and actuators to monitor and modulate the response of structures [1, 2]. Piezoelectric actuators and sensors are innovative for microscopic electromechanical systems and intelligent material systems, particularly in aerospace and medical fields [3]. Conventional piezoelectric sensors and actuators comprise multiple layers of various piezoelectric materials [4–7]. Moreover, piezoelectric layers with uniform material properties are limited by large bending displacement, stress concentration, creeping at high temperature, and failure from interfacial unbounding. All these phenomena are induced by mechanical or electric loading at layer interfaces [8].

To overcome the above limitations, Zhu et al. introduced and fabricated functionally graded piezoelectric material (FGPM) sensors and actuators [9, 10]. FGPMs change nonstop in one or more directions without generating internal stress concentration despite the production of large displacements. Takagi et al. fabricated FGPM bimorph actuators by using a mixed system of lead-zirconate-titanate (PZT) and Pt [11]. Nowadays, FGPMs are widely used intelligent materials for sensors and actuators in microstructural engineering. Many efforts have been made to analyze the behaviors and static/dynamic responses of FGPMs (e.g., shells, beams, and plates), such as the wave propagation study of FGPM plates based on the laminate theory [12]. Moreover, exact 3D analysis of FGPM rectangular plates was conducted by using a state-space approach [13] and to investigate the natural frequencies and mode shapes after being poled perpendicular to the middle plane [14]. The above method was also applied to explore the free vibration of rectangular FGPM plates [15]. The semi-analytical finite element method (FEM) was used to investigate the static response of anisotropic and linear functionally graded magneto-electro-elastic plates [16]. Lezgy-Nazargah et al. [17] carried out static and dynamic

analyses on piezoelectric beams by using a refined sinus model. The results have been found in good agreement with the reference solutions for various electrical and mechanical constrained conditions. Meanwhile, the 3D exact state-space solution [18] and Peano series solution [19] were developed for the cylindrical bending vibration of the FGPM laminates, respectively. Layerwise FEM was adopted to investigate the displacement and stress responses of an FGPM bimorph actuator [20]. Qiu et al. inhibited the vibration of a smart flexible clamped plate by using piezoelectric ceramic patch sensors and actuators [21]. The Timoshenko beam theory was used to analyze the static and dynamic responses of FGPM actuators to thermo-electro-mechanical loading [22]. The first-order shear deformation theory was used to study the static bending, free vibration, and dynamic responses of FGPM plates under electromechanical loading [23]. The free and induced vibrations of FGPM beams under thermo-electro-mechanical loading were characterized using the 3-order shear deformation beam theory [24]. A high-order theory for FGPM shells was proposed based on the generalized Hamilton's principle [8]. Although the FEM (h-version) is adequate for low-frequency vibration analysis, it is not well suited to the vibration analysis of medium- or high-frequency regimes [25]. The spectral finite element method (SFEM) [26, 27] and the weak form quadrature method (QEM) [28, 29] are developed for the dynamic analysis of FGPM beams and structures.

Though FEM is the most widely used and effective numerical approach in practical issues in research and engineering (including mechanics of vibration), it is not necessarily fully perfect or cannot be further improved. For example, the probable overestimation of stiffness in solid structures may lead to locking behavior and inaccurate stress-solving [30]. By adding strain smoothing into FEM [31], Liu et al. established a series of cell-based [32–36], node-based [37, 38], edge-based [39–41], or face-based [42, 43] smoothed FEMs (S-FEMs) and their combinations [44–47]. These S-FEMs with different properties can be used to get desired solutions for a variety of benchmarks and practical mechanic issues [48–50]. The strain-smoothing operations can reduce or alleviate the overstiffness of standard FEM, significantly improving the accuracy of both primal and dual quantities [51]. Moreover, owing to absence of parametric mapping, the shape function derivatives and S-FEM models established in elasticity are not required to be insensitive to mesh distortion [52]. S-FEMs have been successfully extended to analyze the dynamic control of piezoelectric sensors and actuators, topological optimization of linear piezoelectric micromotors, statics, frequency, or defects of smart materials [53–63]. Zheng et al. [64] utilized the cell-based smoothed finite element method with the asymptotic homogenization method to analyze the dynamic issues on micromechanics of piezoelectric composite materials. Zhou et al. [65, 66] deduced the linear and nonlinear cell-based smoothed finite element method of functionally graded magneto-electro-elastic (MEE) structures and further examined the transient responses of MEE sensors or energy harvest structures considering the damping factors. However, there is little literature reported concerning the dynamic response of FGPMs using the electromechanical inhomogeneous cell-based smoothed finite element method. Because of versatility, S-FEMs become convenient and efficient numerical approaches to address different physical issues.

Given the continuous change of the gradient of material properties along the thickness x_3 direction and with cell-based gradient smoothing, we deduced the basic formula of ISFEM and a modified Wilson-θ method to solve the integral solution of the FGPM system. The displacements and potentials of FGPM cantilever beams under sine wave load, cosine wave load, step wave load, and triangular wave load were analyzed in comparison with FEM.

2. Basic Equations for Piezoelectric Materials

2.1. Geometry and Coordinate System. Each beam has a rectangular uniform cross section and is made of N_i layers either completely or partially composed of FGPM beams. The Cartesian coordinate system (x_1, x_2, x_3) and geometric parameters are illustrated in Figure 1.

2.2. Constitutive Equations. At the k-th layer, 3D linear constitutive equations are polarized along its global coordinates as follows:

$$\begin{bmatrix}\sigma_{11}\\ \sigma_{22}\\ \sigma_{33}\\ \sigma_{23}\\ \sigma_{13}\\ \sigma_{12}\end{bmatrix}^{(k)} = \begin{bmatrix} c_{11} & c_{12} & c_{13} & 0 & 0 & 0\\ c_{12} & c_{22} & c_{23} & 0 & 0 & 0\\ c_{13} & c_{23} & c_{33} & 0 & 0 & 0\\ 0 & 0 & 0 & c_{44} & 0 & 0\\ 0 & 0 & 0 & 0 & c_{55} & 0\\ 0 & 0 & 0 & 0 & 0 & c_{66}\end{bmatrix}^{(k)} \begin{bmatrix}\varepsilon_{11}\\ \varepsilon_{22}\\ \varepsilon_{33}\\ 2\varepsilon_{23}\\ 2\varepsilon_{13}\\ 2\varepsilon_{12}\end{bmatrix}^{(k)} - \begin{bmatrix} 0 & 0 & e_{31}\\ 0 & 0 & e_{32}\\ 0 & 0 & e_{33}\\ 0 & e_{24} & 0\\ e_{15} & 0 & 0\\ 0 & 0 & 0\end{bmatrix}^{(k)} \begin{bmatrix}E_1\\ E_2\\ E_3\end{bmatrix}^{(k)}, \tag{1}$$

$$\begin{bmatrix}D_1\\ D_2\\ D_3\end{bmatrix}^{(k)} = \begin{bmatrix} 0 & 0 & 0 & 0 & e_{15} & 0\\ 0 & 0 & 0 & e_{24} & 0 & 0\\ e_{31} & e_{32} & e_{33} & 0 & 0 & 0\end{bmatrix}^{(k)} \begin{bmatrix}\varepsilon_{11}\\ \varepsilon_{22}\\ \varepsilon_{33}\\ 2\varepsilon_{23}\\ 2\varepsilon_{13}\\ 2\varepsilon_{12}\end{bmatrix}^{(k)} + \begin{bmatrix}\chi_{11} & 0 & 0\\ 0 & \chi_{22} & 0\\ 0 & 0 & \chi_{33}\end{bmatrix}^{(k)} \begin{bmatrix}E_1\\ E_2\\ E_3\end{bmatrix}^{(k)}, \tag{2}$$

where σ_{ij} and ε_{kl} are the stress tensor and infinitesimal strain tensor, respectively, E_i and D_i are electric field and electric

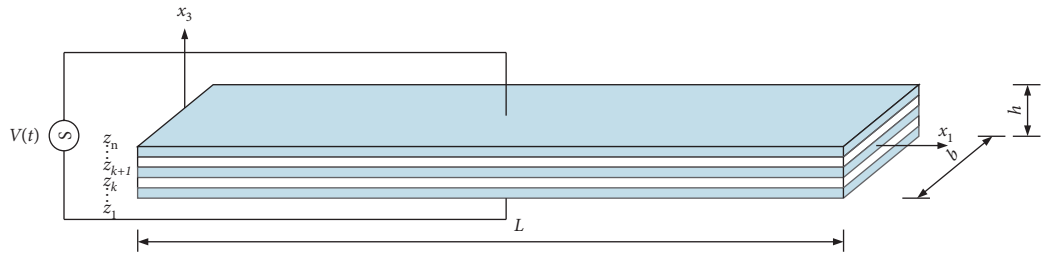

Figure 1: FGPM beams: Cartesian coordinate system and geometric parameters: length (L), width (b), and height (h).

displacement vector components, respectively; e_{ik}, c_{kl}, and X_{ij} are the piezoelectric, elastic, and dielectric material constants, respectively. Different from homogeneous piezoelectric materials, the three constants are dependent on coordinate x_3. We assume that the material properties along the thickness direction are arbitrarily distributed as follows:

$$\begin{aligned} c_{ijkl}(x_3) &= c^0_{ijkl} f(x_3), \\ e_{ikl}(x_3) &= e^0_{ikl} f(x_3), \\ \chi_{ik}(x_3) &= \chi^0_{ik} f(x_3), \quad i,j,k,l == 1,2,3, \end{aligned} \tag{3}$$

where $f(x_3)$ is an arbitrary function and c^0_{kl}, e^0_{kl}, and χ^0_{kl} are values at the plane $x_3 = 0$.

In an FGPM beam, equations (1) and (2) are reduced to

$$\begin{aligned} \overline{\boldsymbol{\sigma}} &= \overline{\mathbf{C}}\overline{\boldsymbol{\varepsilon}} - \overline{\mathbf{e}}\overline{\mathbf{E}}, \\ \overline{\mathbf{D}} &= \overline{\mathbf{e}}^{\mathrm{T}}\overline{\boldsymbol{\varepsilon}} + \overline{\boldsymbol{\chi}}\overline{\mathbf{E}}, \end{aligned} \tag{4}$$

where

$$\begin{aligned} \overline{\boldsymbol{\sigma}} &= \begin{bmatrix} \sigma_{11} \\ \sigma_{33} \\ \sigma_{13} \end{bmatrix}, \\ \overline{\mathbf{C}} &= \begin{bmatrix} c_{11} & c_{13} & 0 \\ c_{31} & c_{33} & 0 \\ 0 & 0 & c_{55} \end{bmatrix}, \\ \overline{\mathbf{e}} &= \begin{bmatrix} 0 & e_{31} \\ 0 & e_{33} \\ e_{15} & 0 \end{bmatrix}, \\ \overline{\mathbf{E}} &= \begin{bmatrix} E_1 \\ E_3 \end{bmatrix}, \\ \overline{\boldsymbol{\varepsilon}} &= \begin{bmatrix} \varepsilon_{11} \\ \varepsilon_{33} \\ \varepsilon_{13} \end{bmatrix}, \\ \overline{\mathbf{D}} &= \begin{bmatrix} D_1 \\ D_3 \end{bmatrix}, \\ \overline{\boldsymbol{\chi}} &= \begin{bmatrix} \chi_{11} & 0 \\ 0 & \chi_{33} \end{bmatrix}. \end{aligned} \tag{5}$$

2.3. Weak Formulation. The principle of virtual work for a piezoelectric medium of volume Ω and regular boundary surface Γ can be written as

$$\begin{aligned} \delta\Pi = \delta U - \delta W = &-\int_\Omega \delta\overline{\boldsymbol{\varepsilon}}^{\mathrm{T}}\overline{\boldsymbol{\sigma}}\, d\Omega + \int_\Gamma \delta\mathbf{u}^{\mathrm{T}}\mathbf{F}_{\mathrm{s}}\, d\Gamma \\ &+ \int_\Omega \delta\mathbf{u}^{\mathrm{T}}\mathbf{F}_{\mathrm{v}}\, d\Omega - \int_\Omega \rho\delta\mathbf{u}^{\mathrm{T}}\ddot{\mathbf{u}}\, d\Omega + \int_\Omega \delta\overline{\mathbf{E}}^{\mathrm{T}}\overline{\mathbf{D}}\, d\Omega \\ &+ \int_\Gamma \overline{Q}\delta\boldsymbol{\varphi}\, d\Gamma - \int_\Omega \overline{q}\delta\boldsymbol{\varphi}\, d\Omega = 0, \end{aligned} \tag{6}$$

where $\mathbf{F}_{\mathrm{s}}$, $\mathbf{F}_{\mathrm{v}}$, $\mathbf{u}$, and $\boldsymbol{\varphi}$ are the vectors of surface force, mechanical body force, node displacements, and node electrical potentials, respectively; $\overline{q}$, $\overline{Q}$, and ρ are the electrical body charge, surface charge, and mass density, respectively; and δ is the virtual quantity.

3. Electromechanical ISFEM

The solving domain Ω is discretized into n_{p} elements, which contain N_{n} nodes; the approximation displacement $\overline{\mathbf{u}}$ and the approximation electrical potential $\overline{\boldsymbol{\varphi}}$ for the FGPM problem can be expressed as

$$\begin{aligned} \overline{\mathbf{u}} &= \sum_{i=1}^{n_{\mathrm{p}}} N_i^{\mathrm{u}} u_i = \mathbf{N}_{\mathrm{u}}\mathbf{u}, \\ \overline{\boldsymbol{\varphi}} &= \sum_{i=1}^{n_{\mathrm{p}}} N_i^{\varphi} \varphi_i = \mathbf{N}_{\varphi}\boldsymbol{\varphi}, \end{aligned} \tag{7}$$

where $\mathbf{N}_{\mathrm{u}}$ and $\mathbf{N}_{\varphi}$ are the ISFEM displacement shape function and electrical potential shape function, respectively.

Four-node element is divided into four smoothing subdomains. Field nodes, edge smoothing nodes, center smoothing nodes and edge Gaussian points, the outer normal vector distribution, and the shape function values are shown in Figure 2.

At any point $\mathbf{x}^k$ in the smoothing subdomains Ω_i^k, the smoothed strain $\overline{\boldsymbol{\varepsilon}}(\mathbf{x}^k)$ and the smoothed electric field $\overline{E}(\mathbf{x}^k)$ are

$$\overline{\boldsymbol{\varepsilon}}\left(\mathbf{x}^k\right) = \int_{\Omega_i^k} \boldsymbol{\varepsilon}(\mathbf{x})\Phi\left(\mathbf{x} - \mathbf{x}^k\right) d\Omega, \tag{8}$$

$$\overline{\mathbf{E}}\left(\mathbf{x}^k\right) = \int_{\Omega_i^k} \mathbf{E}(\mathbf{x})\Phi\left(\mathbf{x} - \mathbf{x}^k\right) d\Omega, \tag{9}$$

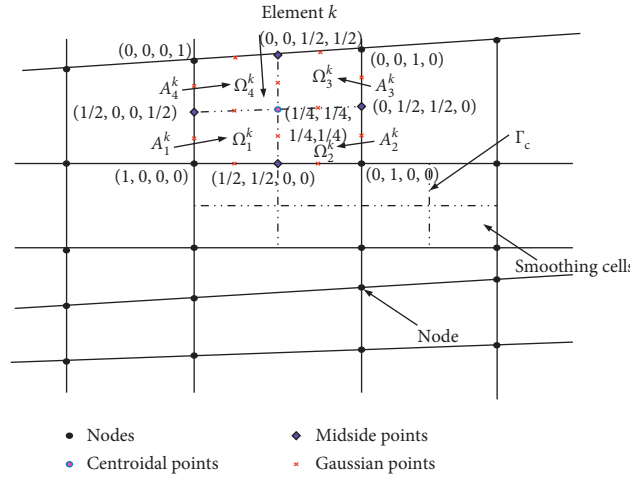

FIGURE 2: Smoothing subcells and the values of shape functions (reproduced from Zheng et al. [64] under the Creative Commons Attribution License/public domain).

where $\boldsymbol{\varepsilon}(\mathbf{x})$ and $\mathbf{E}(\mathbf{x})$ are the strain and electric field in FEM, respectively, and $\Phi(\mathbf{x}-\mathbf{x}^k)$ is the constant function:

$$\Phi\left(\mathbf{x}-\mathbf{x}^k\right)=\begin{cases}\dfrac{1}{A_i^k}, & \mathbf{x}\in\Omega_i^k,\\[2ex] 0, & \mathbf{x}\notin\Omega_i^k,\end{cases} \tag{10}$$

where

$$A_i^k=\int_{\Omega_i^k} d\Omega. \tag{11}$$

Substituting equation (10) into equations (8) and (9), then we have

$$\overline{\boldsymbol{\varepsilon}}\left(\mathbf{x}^k\right)=\frac{1}{A_i^k}\int_{\Gamma_i^k}\mathbf{n}_{\mathrm{u}}^k\mathbf{u}\,d\Gamma, \tag{12}$$

$$\overline{\mathbf{E}}\left(\mathbf{x}^k\right)=\frac{1}{A_i^k}\int_{\Gamma_i^k}\mathbf{n}_{\varphi}^k\boldsymbol{\varphi}\,d\Gamma, \tag{13}$$

where Γ_i^k is the boundary of Ω_i^k and $\mathbf{n}_{\mathrm{u}}^k$ and $\mathbf{n}_{\varphi}^k$ are the outer normal vector matrixes of the smoothing domain boundary

$$\mathbf{n}_{\mathrm{u}}^k=\begin{bmatrix} n_{x_1}^k & 0\\ 0 & n_{x_3}^k\\ n_{x_3}^k & n_{x_1}^k\end{bmatrix},\qquad \mathbf{n}_{\varphi}^k=\begin{bmatrix} n_{x_1}^k\\ n_{x_3}^k\end{bmatrix}. \tag{14}$$

Equations (12) and (13) can be rewritten as

$$\overline{\boldsymbol{\varepsilon}}\left(\mathbf{x}^k\right)=\sum_{i=1}^{n_e}\overline{\mathbf{B}}_{\mathrm{u}}^i\left(\mathbf{x}^k\right)\mathbf{u}_i,\qquad \overline{\mathbf{E}}\left(\mathbf{x}^k\right)=-\sum_{i=1}^{n_e}\overline{\mathbf{B}}_{\varphi}^i\left(\mathbf{x}^k\right)\boldsymbol{\varphi}_i, \tag{15}$$

where n_e is the number of smoothing elements.

$$\overline{\mathbf{B}}_{\mathrm{u}}^i\left(\mathbf{x}^k\right)=\frac{1}{A_i^k}\int_{\Gamma^k}\begin{bmatrix} N_i^{\mathrm{u}}n_{x_1}^k & 0\\ 0 & N_i^{\mathrm{u}}n_{x_3}^k\\ N_i^{\mathrm{u}}n_{x_3}^k & N_i^{\mathrm{u}}n_{x_1}^k\end{bmatrix}d\Gamma, \tag{16}$$

$$\overline{\mathbf{B}}_{\varphi}^i\left(\mathbf{x}^k\right)=\frac{1}{A_i^k}\int_{\Gamma^k}\begin{bmatrix} N_i^{\varphi}n_{x_1}^k\\ N_i^{\varphi}n_{x_3}^k\end{bmatrix}d\Gamma. \tag{17}$$

At the Gaussian point $\mathbf{x}_b^{\mathrm{G}}$, equations (16) and (17) are

$$\overline{\mathbf{B}}_{\mathrm{u}}^i\left(\mathbf{x}^k\right)=\frac{1}{A_i^k}\sum_{b=1}^{n_b}\begin{pmatrix} N_i^{\mathrm{u}}(\mathbf{x}_b^{\mathrm{G}})n_{x_1}^k & 0\\ 0 & N_i^{\mathrm{u}}(\mathbf{x}_b^{\mathrm{G}})n_{x_3}^k\\ N_i^{\mathrm{u}}(\mathbf{x}_b^{\mathrm{G}})n_{x_3}^k & N_i^{\mathrm{u}}(\mathbf{x}_b^{\mathrm{G}})n_{x_1}^k\end{pmatrix}l_b^k,$$

$$\overline{\mathbf{B}}_{\varphi}^i\left(\mathbf{x}^k\right)=\frac{1}{A_i^k}\sum_{b=1}^{n_b}\begin{pmatrix} N_i^{\varphi}(\mathbf{x}_b^{\mathrm{G}})n_{x_1}^k\\ N_i^{\varphi}(\mathbf{x}_b^{\mathrm{G}})n_{x_3}^k\end{pmatrix}l_b^k, \tag{18}$$

where $\mathbf{x}_b^{\mathrm{G}}$ and l_b^k are the Gaussian point and the length of the smoothing boundary, respectively, and n_b is the total number of boundaries for each smoothing subdomain. As the shape function is linearly changed along each side of the smoothing subdomain, one Gauss point is sufficient for accurate boundary integration [30].

The essential distinction between ISFEM and FEM is that FEM needs to construct the shape function matrix of the element, while ISFEM only needs to use the shape function at the Gaussian point of the smoothing element boundary and does not require to involve the shape function derivatives. The above can reduce the continuity requirement of the shape function, and therefore, the accuracy and convergence of the method are improved.

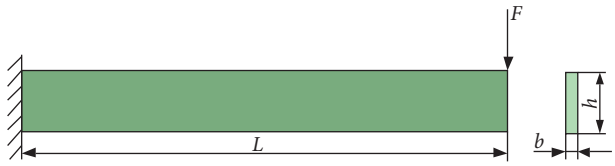

Figure 3: Geometry of the cantilever beam.

Table 1: Material constants.

Material	c_{11} (GPa)	c_{12} (GPa)	c_{13} (GPa)	c_{33} (GPa)	c_{44} (GPa)	ρ (kg/m^3)	e_{31} (C/m^2)	e_{33} (C/m^2)	e_{15} (C/m^2)	χ_{11}/χ_0	χ_{33}/χ_0	χ_0 (C/N·m^2)
PZT-4	139.0	77.80	74.30	115.0	25.60	7600	−5.20	15.10	12.70	1476.0	1301.0	8.854×10^{-12}
PZT-5H	126.0	79.60	84.10	114.0	23.30	7500	−6.50	17.44	23.30	1468.9	1698.3	8.854×10^{-12}

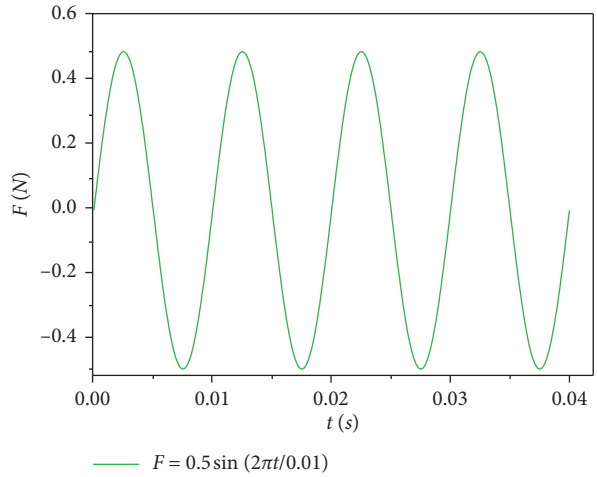

Figure 4: Sine wave load.

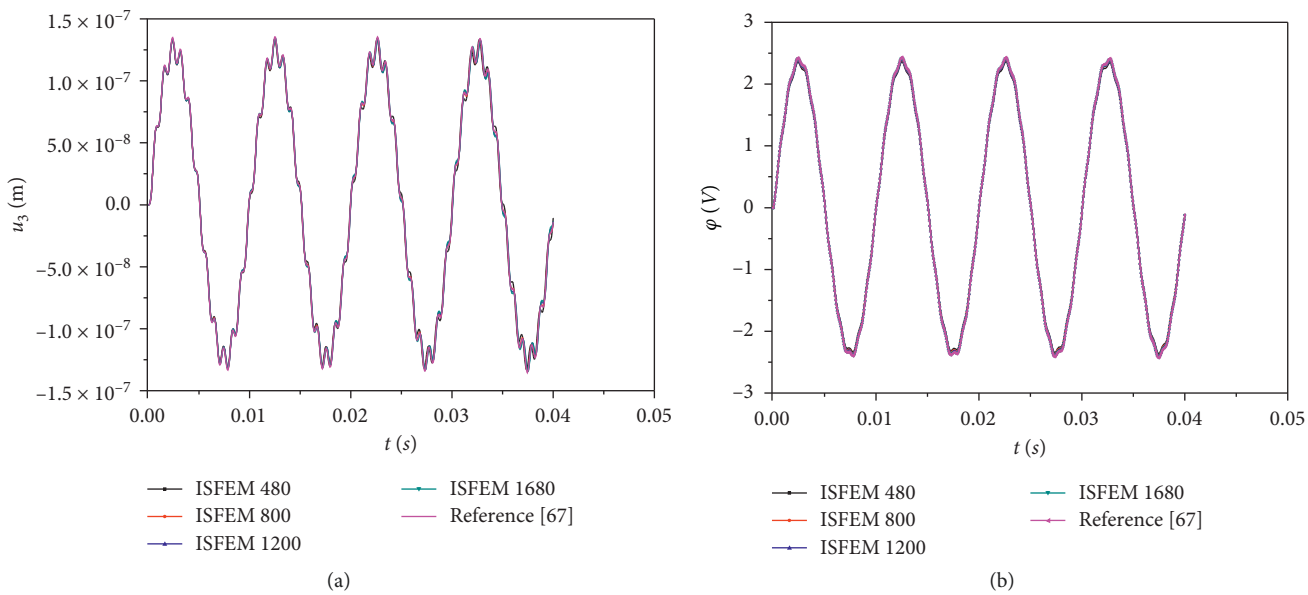

Figure 5: Variations of the displacement u_3 and electrical potential φ at the loading point with time when the gradient parameter was $n = -5$. (a) Displacement. (b) Electrical potential.

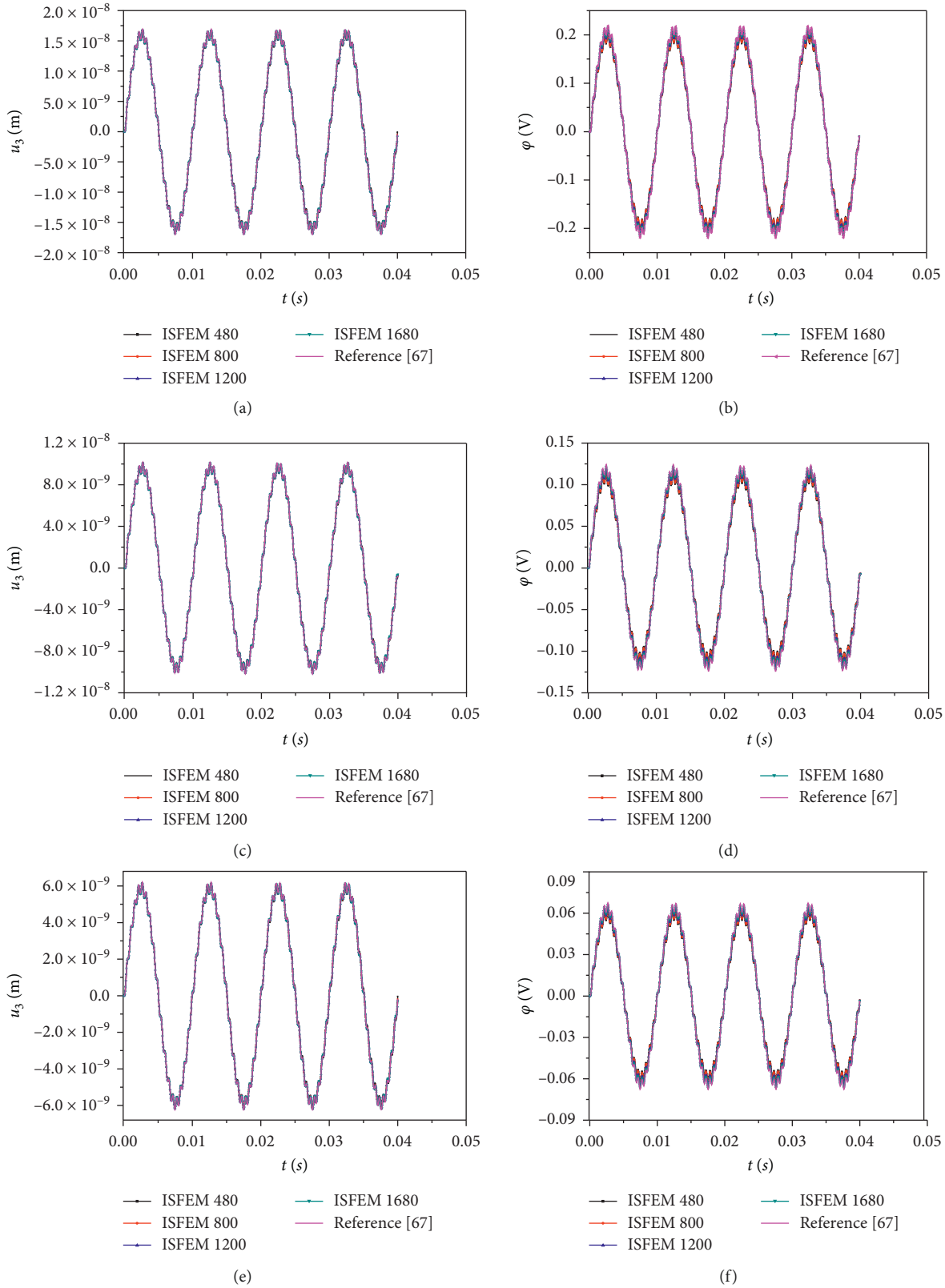

Figure 6: Continued.

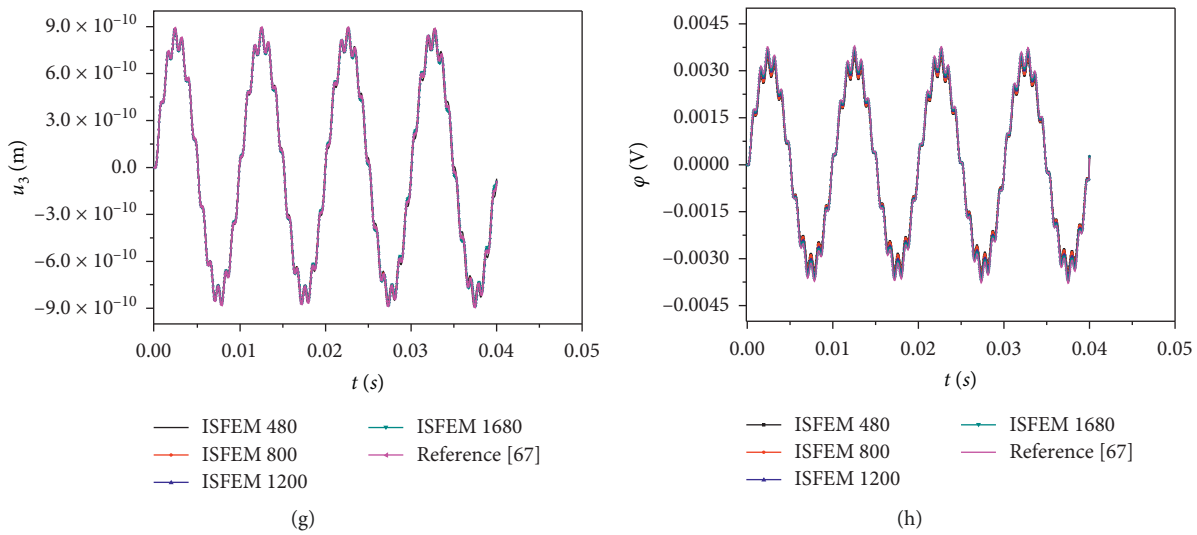

FIGURE 6: Variations of the displacement u_3 and electrical potential φ at the loading point with time when the gradient parameter was $n = -1$, 0, 1, and 5. (a) Displacement ($n = -1$). (b) Electrical potential ($n = -1$). (c) Displacement ($n = 0$). (d) Electrical potential ($n = 0$). (e) Displacement ($n = 1$). (f) Electrical potential ($n = 1$). (g) Displacement ($n = 5$). (h) Electrical potential ($n = 5$).

The dynamic model of the FGPM electromechanical system can be derived from the Hamilton principle in the following form:

$$\overline{\mathbf{M}}\ddot{\mathbf{q}} + \overline{\mathbf{K}}\mathbf{q} = \overline{\mathbf{F}}, \tag{19}$$

where

$$\overline{\mathbf{M}} = \begin{bmatrix} \mathbf{M}_{uu} & 0 \\ 0 & 0 \end{bmatrix},$$

$$\ddot{\mathbf{q}} = \begin{Bmatrix} \ddot{\mathbf{u}} \\ \ddot{\boldsymbol{\varphi}} \end{Bmatrix},$$

$$\overline{\mathbf{K}} = \begin{bmatrix} \mathbf{K}_{uu} & \mathbf{K}_{u\varphi} \\ \mathbf{K}_{u\varphi}^{T} & \mathbf{K}_{\varphi\varphi} \end{bmatrix},$$

$$\mathbf{q} = \begin{Bmatrix} \mathbf{u} \\ \boldsymbol{\varphi} \end{Bmatrix}, \tag{20}$$

$$\overline{\mathbf{F}} = \begin{Bmatrix} \mathbf{F} \\ \mathbf{Q} \end{Bmatrix},$$

$$\mathbf{M}_{uu} = \sum_{e} \mathbf{M}_{uu}^{e},$$

$$\mathbf{M}_{uu}^{e} = \operatorname{diag}\{m_1, m_1, m_2, m_2, m_3, m_3, m_4, m_4\},$$

where $m_i = p_i T$, A_i^k ($i = 1, 2, 3, 4$) is the mass of the i-th smoothing element corresponding to node i, T is the smoothing element thickness, and p_i is the density of Gaussian integration point of the i-th smoothing subdomain:

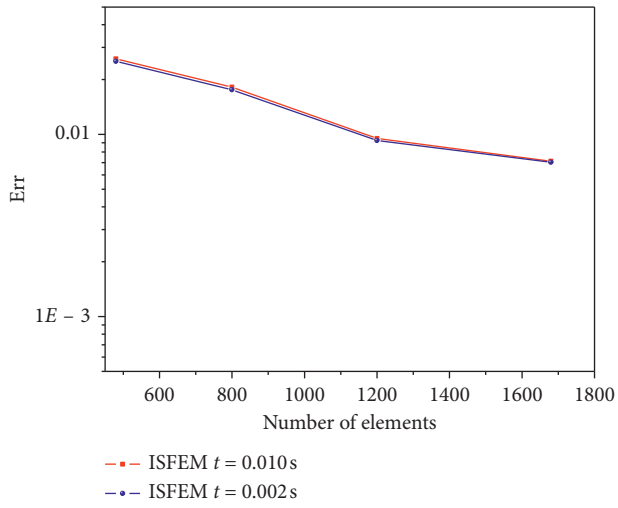

FIGURE 7: Convergence rate of ISFEM.

$$\mathbf{K}_{uu} = \sum_{i=1}^{n_c} \overline{\mathbf{B}}_{u}^{iT} \overline{\mathbf{C}\mathbf{B}}_{u}^{i} A_i^k,$$

$$\mathbf{K}_{u\varphi} = \sum_{i=1}^{n_c} \overline{\mathbf{B}}_{u}^{iT} \overline{\mathbf{e}\mathbf{B}}_{\varphi}^{i} A_i^k,$$

$$\mathbf{K}_{\varphi\varphi} = -\sum_{i=1}^{n_c} \overline{\mathbf{B}}_{\varphi}^{iT} \overline{\boldsymbol{\chi}\mathbf{B}}_{\varphi}^{i} A_i^k, \tag{21}$$

$$\mathbf{F} = \int_{\Omega} \mathbf{N}_{u}^{T} \mathbf{F}_{v}\, d\Omega - \int_{\Gamma_q} \mathbf{N}_{u}^{T} \mathbf{F}_{s}\, d\Gamma,$$

$$\mathbf{Q} = \int_{\Omega} \mathbf{N}_{\varphi}^{T} \overline{Q}\, d\Omega + \int_{\Gamma_q} \mathbf{N}_{\varphi}^{T} \overline{q}\, d\Gamma,$$

where $n_c = n_p \times n_e$.

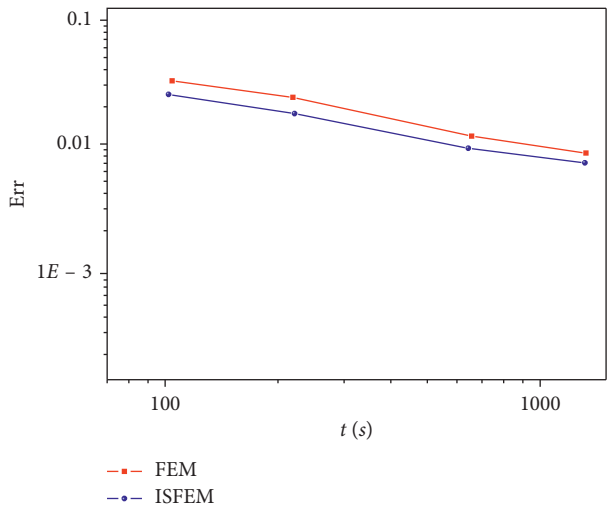

Figure 8: Comparison of computational efficiency.

Table 2: Displacement u_3 and electrical potential φ at the loading point with the gradient parameter $n = -5, -1, 0, 1$, and 5 of the FGPM beam based on PZT-4.

Time (s)	Field variables	$n=-5$		$n=-1$		$n=0$		$n=1$		$n=5$	
		ISFEM	FEM	ISFEM	FEM	ISFEM	FEM	ISFEM	FEM	ISFEM	FEM
0.0001	$u_3 \times 10^{-10}$ m	12.852	12.658	2.760	2.751	1.707	1.702	1.006	1.004	0.0756	0.0754
	$\varphi \times 10^{-2}$ V	11.848	11.912	0.442	0.427	0.212	0.207	0.0961	0.0944	0.00112	0.00110
0.0004	$u_3 \times 10^{-9}$ m	28.517	28.367	4.735	4.715	2.855	2.842	1.738	1.731	0.187	0.187
	$\varphi \times 10^{-1}$ V	5.851	5.747	0.597	0.582	0.349	0.339	0.193	0.188	0.0805	0.782
0.0025	$u_3 \times 10^{-8}$ m	13.345	13.191	1.538	1.528	0.917	0.913	0.564	0.561	0.0882	0.0873
	φ (V)	2.447	2.391	0.198	0.191	0.112	0.109	0.0621	0.0605	0.00386	0.00372
0.004	$U_3 \times 10^{-9}$ m	77.799	77.682	10.154	10.146	6.165	6.123	3.727	3.725	0.514	0.516
	φ (V)	1.434	1.406	0.129	0.125	0.0756	0.0740	0.0414	0.0401	0.00224	0.00221

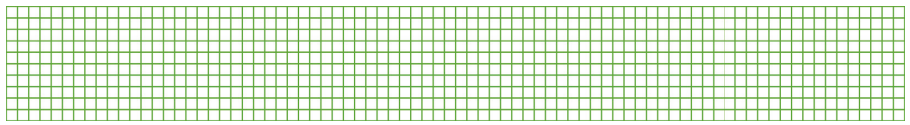

Figure 9: Mesh of the FGPM beam.

Table 3: Displacement u_3 and electrical potential φ at the loading point with the gradient parameter $n = -5, -1, 0, 1$, and 5 of the FGPM beam based on PZT-5H.

Time (s)	Field variables	$n=-5$		$n=-1$		$n=0$		$n=1$		$n=5$	
		ISFEM	FEM	ISFEM	FEM	ISFEM	FEM	ISFEM	FEM	ISFEM	FEM
0.0001	$u_3 \times 10^{-10}$ m	13.691	13.424	2.951	2.942	1.826	1.821	1.076	1.074	0.0802	0.0800
	$\varphi \times 10^{-2}$ V	12.098	12.493	0.413	0.403	0.190	0.194	0.0825	0.0843	0.000624	0.000649
0.0004	$u_3 \times 10^{-9}$ m	31.394	31.196	5.583	5.561	3.381	3.367	2.050	2.042	0.207	0.206
	$\varphi \times 10^{-1}$ V	5.901	6.057	0.599	0.607	0.349	0.350	0.192	0.190	0.0736	0.0735
0.0025	$u_3 \times 10^{-8}$ m	16.122	16.006	2.017	2.003	1.118	1.117	0.741	0.736	0.107	0.106
	φ (V)	2.522	2.584	0.219	0.219	0.122	0.123	0.0691	0.0689	0.00392	0.00393
0.004	$u_3 \times 10^{-9}$ m	76.019	75.052	10.339	10.264	6.264	6.261	3.795	3.768	0.501	0.496
	φ (V)	1.402	1.437	0.113	0.113	0.0649	0.0653	0.0351	0.0350	0.00179	0.00178

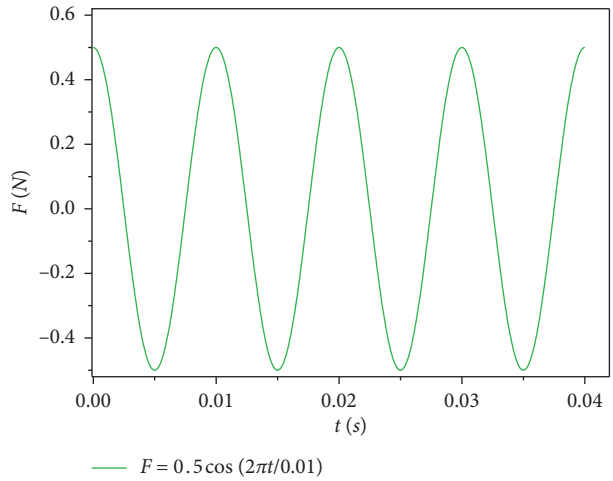

Figure 10: Cosine wave load.

Table 4: Displacement u_3 and electrical potential φ at the loading point with the gradient parameter $n = -5, -1, 0, 1$, and 5 of the FGPM beam based on PZT-4 under cosine load.

Time (s)	Field variables	$n=-5$		$n=-1$		$n=0$		$n=1$		$n=5$	
		ISFEM	FEM	ISFEM	FEM	ISFEM	FEM	ISFEM	FEM	ISFEM	FEM
0.0001	$u_3\times10^{-9}$ m	20.427	20.159	4.387	4.382	2.713	2.710	1.600	1.599	0.120	0.120
	$\varphi\times10^{-2}$ V	188.326	189.821	7.029	6.896	3.369	3.269	1.528	1.5044	0.0178	0.0175
0.0004	$u_3\times10^{-8}$ m	21.208	21.234	2.738	2.743	1.610	1.611	1.006	1.004	0.141	0.142
	$\varphi\times10^{-1}$ V	27.889	27.949	3.315	3.216	0.193	0.187	1.113	1.098	0.0648	0.0639
0.0025	$u_3\times10^{-9}$ m	−33.487	−32.845	−12.058	−11.952	−4.445	−4.345	−4.436	−4.392	−0.225	−0.221
	φ (V)	−0.138	−0.137	−0.132	−0.128	−0.0491	−0.0479	−0.0486	−0.0470	−0.00086	−0.00085
0.004	$u_3\times10^{-9}$ m	−11.111	−11.501	−0.984	−0.969	−5.549	−5.616	−0.351	−0.339	−0.0981	−0.0913
	φ (V)	−1.408	−1.365	−0.0176	−0.0174	−0.0653	−0.0635	0.00234	0.00229	0.000596	0.000579

Table 5: Displacement u_3 and electrical potential φ at the loading point with the gradient parameter $n = -5, -1, 0, 1$, and 5 of the FGPM beam based on PZT-5H under cosine load.

Time (s)	Field variables	$n=-5$		$n=-1$		$n=0$		$n=1$		$n=5$	
		ISFEM	FEM	ISFEM	FEM	ISFEM	FEM	ISFEM	FEM	ISFEM	FEM
0.0001	$u_3\times10^{-9}$ m	2.902	2.901	4.691	4.685	2.902	2.901	1.710	1.710	0.128	0.127
	$\varphi\times10^{-2}$ V	192.287	198.967	6.561	6.742	3.017	3.092	1.312	1.342	0.00992	0.0101
0.0004	$u_3\times10^{-8}$ m	23.941	23.948	3.486	3.493	2.069	2.064	1.281	1.284	0.160	0.159
	$\varphi\times10^{-1}$ V	28.178	29.094	3.5841	3.613	2.108	2.121	1.203	1.201	0.0621	0.0616
0.0025	$u_3\times10^{-9}$ m	117.958	122.357	−4.831	−4.723	−7.090	−6.942	−1.777	−1.715	0.795	0.8136
	φ (V)	0.50863	0.5017	−0.0407	−0.0393	−0.0688	−0.0652	−0.0151	−0.0148	0.00338	0.00342
0.004	$u_3\times10^{-9}$ m	−183.26	−179.45	−27.847	−27.063	−9.636	−9.387	−10.233	−9.998	−1.287	−1.263
	φ (V)	−2.273	−2.176	−0.284	−0.277	−0.0931	−0.0885	−0.0951	−0.0949	−0.00466	−0.00451

The application of the inhomogeneous smoothing element is to calculate stiffness matrix of the element. The parameters of four smoothing subdomains A_i^k $(i = 1, 2, 3, 4)$ are various in the elements, so the actual parameters at the Gaussian integration point are taken directly in order to reflect the changes of material property in each element.

4. Modified Wilson-θ Method

The modified Wilson-θ method is an important scheme and an implicit integral way to solve the dynamic system equations [63]. If $\theta > 1.37$, the solution is unconditionally stable. The detailed procedures are showed as follows:

4.1. Initial Calculation

(1) Formulate generalized stiffness matrix $\overline{\mathbf{K}}$, mass matrix $\overline{\mathbf{M}}$, and damping matrix $\overline{\mathbf{C}}$

(2) Calculate initial values of $\mathbf{q}$, $\dot{\mathbf{q}}$, $\ddot{\mathbf{q}}$

(3) Select the time step Δt and the integral constant θ $(\theta = 1.4)$

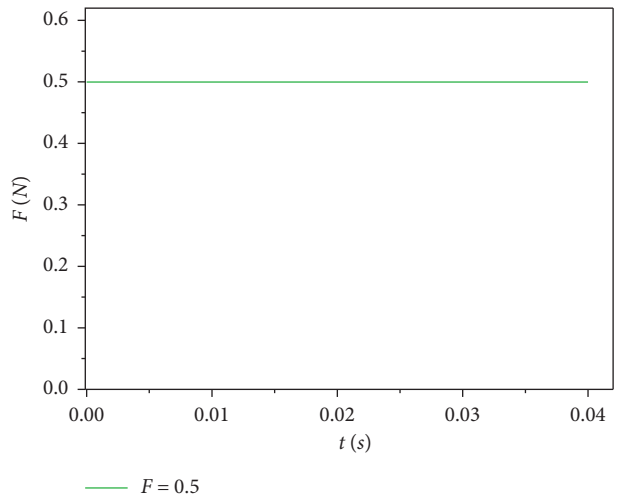

Figure 11: Step wave load.

$$
\begin{aligned}
a_0 &= \frac{6}{(\theta\Delta t)^2},\\
a_1 &= \frac{3}{(\theta\Delta t)},\\
a_2 &= 2a_1,\\
a_3 &= \frac{\theta\Delta t}{2},\\
a_4 &= \frac{a_0}{\theta},\\
a_5 &= -\left(\frac{a_2}{\theta}\right),\\
a_6 &= 1-\frac{3}{\theta},\\
a_7 &= \frac{\Delta t}{2},\\
a_8 &= \frac{\Delta t^2}{6}.
\end{aligned}
\tag{22}
$$

(4) Formulate an effective generalized stiffness matrix $\widetilde{\mathbf{K}}$:
$\widetilde{\mathbf{K}} = \overline{\mathbf{K}} + a_0\overline{\mathbf{M}} + a_1\overline{\mathbf{C}}$

4.2. For Each Time Step

(1) Calculate the payload at time $t+\theta\Delta t$:

$$
\begin{aligned}
\widetilde{\mathbf{F}}^{*}_{t+\theta\Delta t} &= \overline{\mathbf{F}}_t + \theta\left(\overline{\mathbf{F}}_{t+\Delta t} - \overline{\mathbf{F}}_t\right)\\
&\quad + \overline{\mathbf{M}}\left(a_0\mathbf{q}_t + a_2\dot{\mathbf{q}}_t + 2\ddot{\mathbf{q}}_t\right)\\
&\quad + \overline{\mathbf{C}}\left(a_1\mathbf{q}_t + 2\dot{\mathbf{q}}_t + a_3\ddot{\mathbf{q}}_t\right).
\end{aligned}
\tag{23}
$$

(2) Calculate the generalized displacement at time $t+\theta\Delta t$:

$$
\widetilde{\mathbf{K}}\mathbf{q}_{t+\theta\Delta t} = \widetilde{\mathbf{F}}^{*}_{t+\theta\Delta t}.
\tag{24}
$$

(3) Calculate the generalized acceleration, generalized speed, and generalized displacement at time $t+\Delta t$:

$$
\begin{aligned}
\ddot{\mathbf{q}}_{t+\Delta t} &= a_4\left(\mathbf{q}_{t+\theta\Delta t} - \mathbf{q}_t\right) + a_5\dot{\mathbf{q}}_t + a_6\ddot{\mathbf{q}}_t,\\
\dot{\mathbf{q}}_{t+\Delta t} &= \dot{\mathbf{q}}_t + a_7\left(\ddot{\mathbf{q}}_{t+\Delta t} + \ddot{\mathbf{q}}_t\right),\\
\mathbf{q}_{t+\Delta t} &= \mathbf{q}_t + \Delta t\dot{\mathbf{q}}_t + a_8\left(\ddot{\mathbf{q}}_{t+\Delta t} + 2\ddot{\mathbf{q}}_t\right).
\end{aligned}
\tag{25}
$$

5. Numerical Examples

Four numerical examples were conducted under sine wave load, cosine wave load, step wave load and triangular wave load, respectively. FGPM cantilever beams of the same dimensions (length $L = 40$ mm, width $h = 5$ mm and thickness $b = 1$ mm) were subjected to forced vibration (Figure 3). The material constants are shown in Table 1. And initial conditions were $\mathbf{q} = 0$ and $\dot{\mathbf{q}} = 0$ at $t = 0$ moment. The FGPM beams were made of PZT-4 or PZT-5H on basis of exponentially graded piezoelectric materials with the following material properties:

$$
\begin{aligned}
c_{kl}(x_3) &= c^0_{kl} f(x_3),\\
e_{kl}(x_3) &= e^0_{kl} f(x_3),\\
\chi_{kl}(x_3) &= \chi^0_{kl} f(x_3),
\end{aligned}
\tag{26}
$$

where $f(x_3) = e^{nx_3/h}$ and n is the gradient parameter.

5.1. Sine Wave Load. The load F applied to the free end and the load waveform is demonstrated in Figure 4. A convergence investigation with respect to meshes was first carried out. Four smoothing subcells were used for electromechanical ISFEM with $\Delta t = 1\times10^{-3}$ s. The variations of displacement u_3 and electrical potential φ at the loading point of the PZT-4-based FGPM beam combined with respect to time are shown in Figure 5. The results at $n = -5$ with the element number of 480, 800, 1200, or 1680 were compared with the reference solution [67]. The variations of u_3 and φ at the loading point combined with respect to time at $n = -1$, 0, 1, and 5 in comparison with the reference solution are shown in Figure 6 [67]. Figure 7 illustrates the total energy norm Err versus the mesh density at $t = 0.002$ s

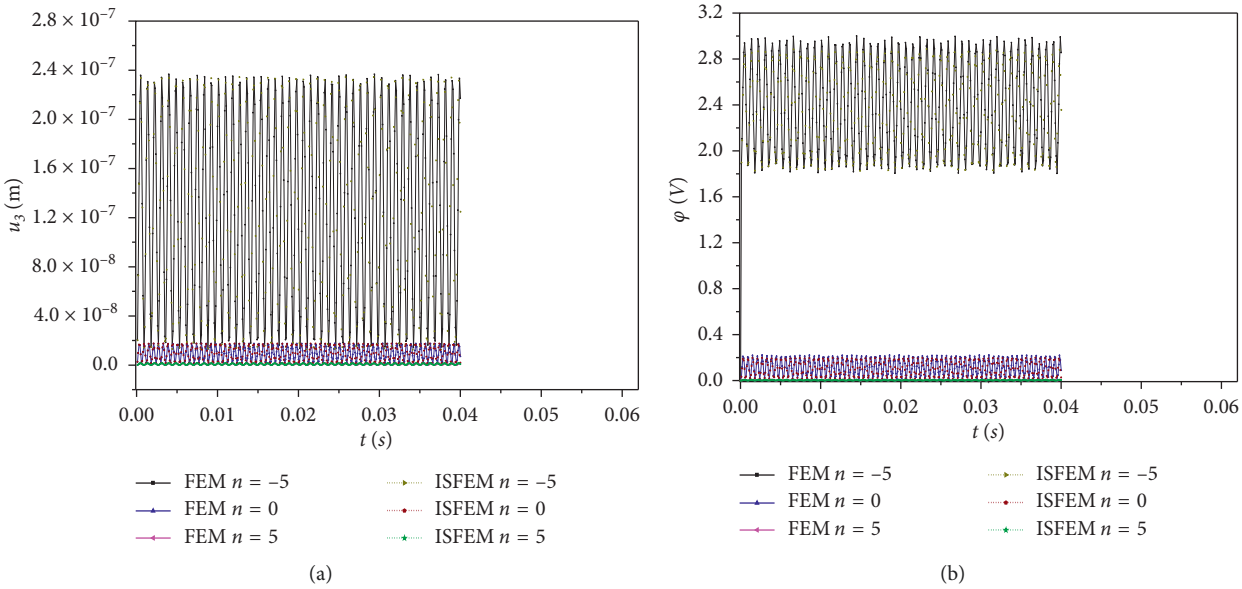

FIGURE 12: Variations of displacement u_3 and electrical potential φ at the loading point with time of the FGPM beam based on PZT-4 when the gradient parameter was $n = -5$, 0 and 5 under step load. (a) Displacement. (b) Electrical potential.

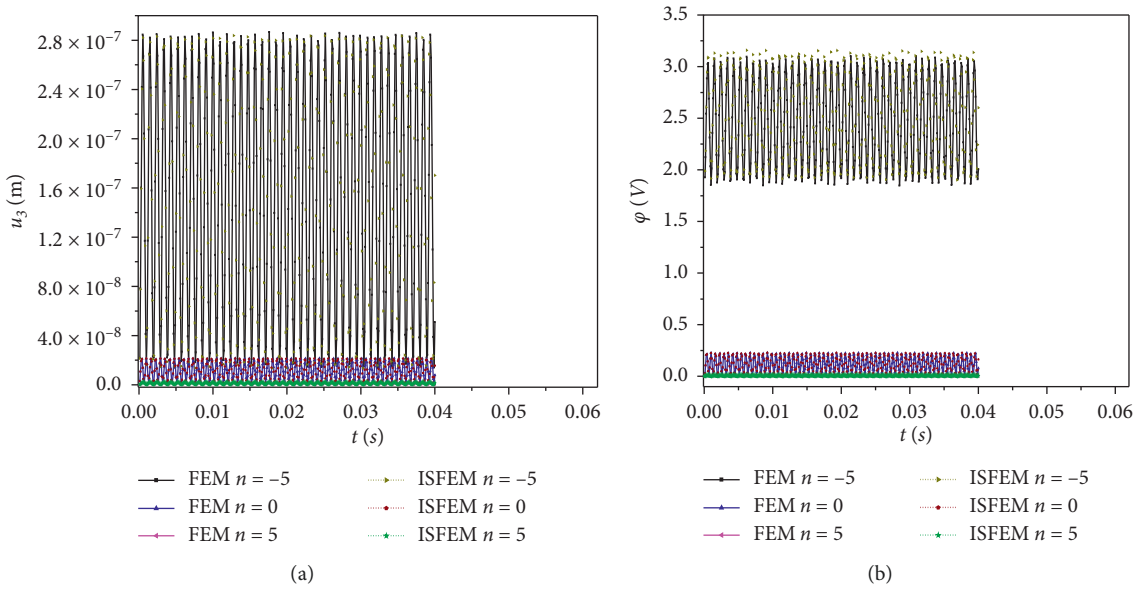

FIGURE 13: Variations of displacement u_3 and electrical potential φ at the loading point with time of the FGPM beam based on PZT-5H when the gradient parameter was $n = -5$, 0 and 5 under step load. (a) Displacement. (b) Electrical potential.

and $t = 0.01$ s. The simulation results are well consistent among different numbers of meshes, which demonstrate the high convergence of ISFEM.

Figure 8 shows a comparison of calculation time between ISFEM and FEM at Intel ® Xeon ® CPU E3-1220 v3 @ 3.10 GHz, 16GB RAM. The bandwidth of the system matrices for the FEM and ISFEM is identical. However, in the ISFEM, only the values of shape functions (not the derivatives) at the quadrature points are needed and the requirement of traditional coordinate transform procedure is not necessary to perform the numerical integration. Therefore, the ISFEM generally needs less computational cost than the FEM for handling the dynamic analysis problems.

The variations of u_3 and φ at the loading point combined with $t = 0.0001$ s, 0.0004 s, 0.0025 s, and 0.004 s in the PZT-4-based FGPM cantilever beam are shown in Table 2. The 80×10 meshes of ISFEM at $n = -5$, -1, 0, 1, and 5 are shown in Figure 9, and FEM is considered 160×20 elements. Clearly, the results of ISFEM with 80×10 elements are the same as the calculated results of FEM using 160×20 elements, suggesting ISFEM has higher accuracy.

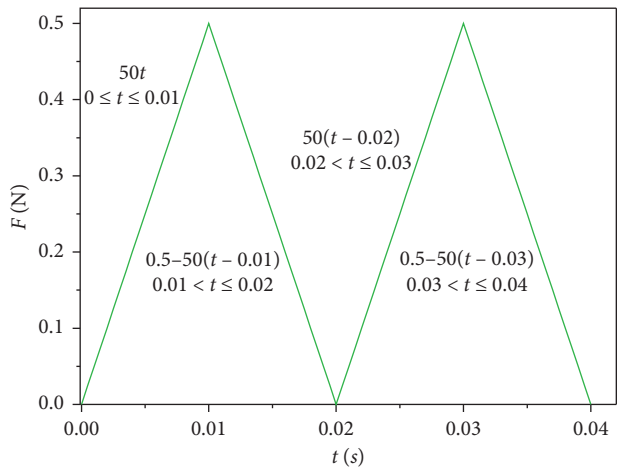

Figure 14: Triangular wave load.

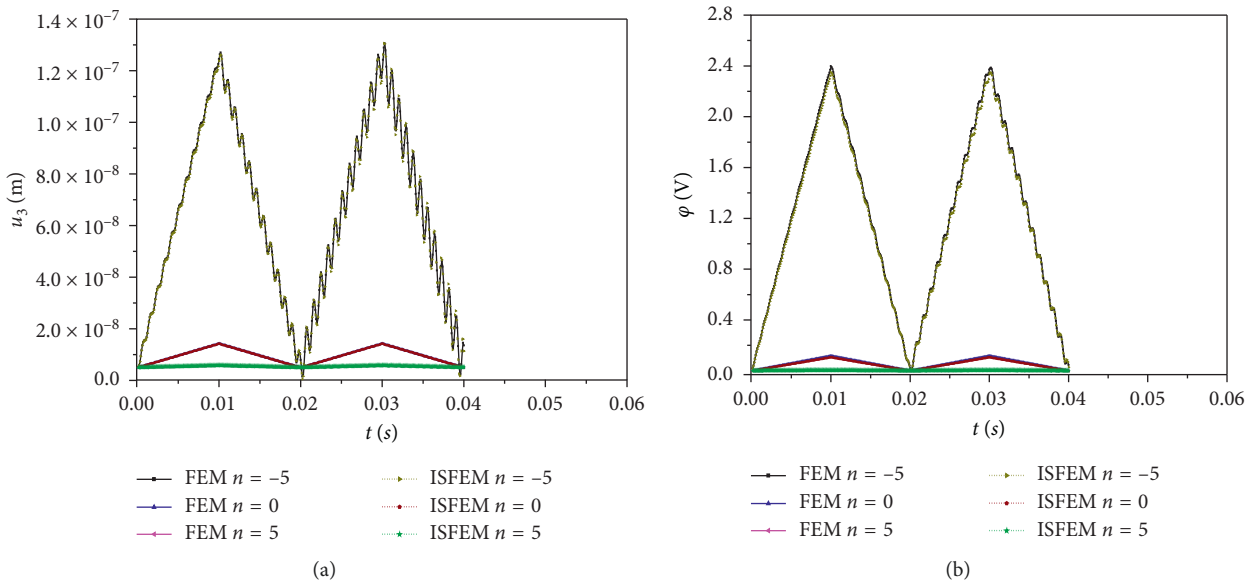

Figure 15: Variations of displacement u_3 and electrical potential φ at the loading point with time of the FGPM beam based on PZT-4 when the gradient parameter was $n = -5$, 0, and 5 under triangular load. (a) Displacement. (b) Electrical potential.

The variations of u_3 and φ at the loading point combined with time of the PZT-5H-based FGPM cantilever beam are listed in Table 3. Clearly, when n changes from −5 to 5, the maximum u_3 and φ decrease, which is consistent with the PZT-4-based FGPM cantilever beam. Furthermore, the results of ISFEM with 80×10 elements are the same as the calculated results of FEM using 160×20 elements, suggesting ISFEM has higher accuracy.

5.2. Cosine Wave Load. The cosine load F applied to the free end and load waveform is shown in Figure 10. The variations of u_3 and φ at the loading point combined with time of PZT-4- and PZT-5H-based FGPM cantilever beams are listed in Tables 4 and 5, respectively. The calculated results of ISFEM with 80×10 elements are the same as those of FEM using 160×20 elements, implying that ISFEM possesses higher accuracy.

5.3. Step Wave Load. The step load F applied to the free end and load waveform is indicated in Figure 11. The variations of u_3 and φ at the loading point combined with time of PZT-4- and PZT-5H-based FGPM cantilever beams are illustrated in Figures 12 and 13, respectively. It is clearly shown that ISFEM possesses higher accuracy than FEM for the calculated results of ISFEM using 80×10 elements are the same as FEM using 160×20 elements.

5.4. Triangular Wave Load. The triangular load F applied to the free end and load waveform is shown in Figure 14. The

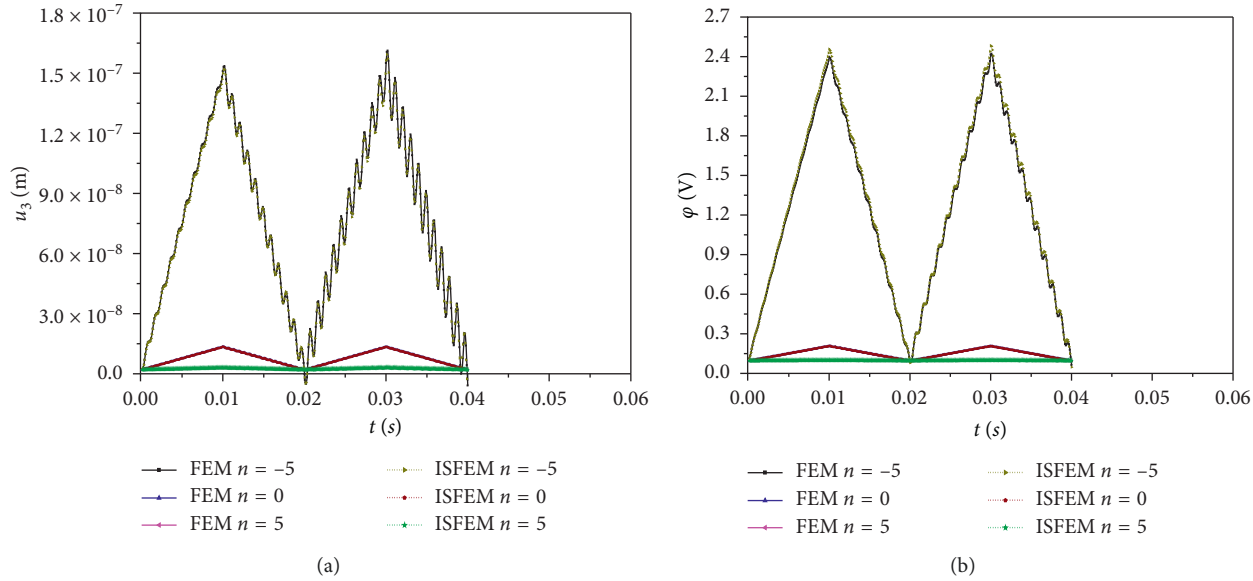

FIGURE 16: Variations of the displacement u_3 and electrical potential φ at the loading point with time of the FGPM beam based on PZT-5H when the gradient parameter was $n = -5$, 0, and 5 under triangular load. (a) Displacement. (b) Electrical potential.

variations of u_3 and φ at the loading point combined with time of PZT-4- and PZT-5H-based FGPM cantilever beams are shown in Figures 15 and 16, respectively. It shows that the solutions of CS-FEM with less elements are the same as the solutions of FEM using more elements.

6. Conclusions

An electromechanical ISFEM was proposed given the continuous changes of the gradient of material properties along the thickness x_3 direction and with cell-based gradient smoothing. The modified Wilson-θ method was deduced to solve the integral solution of the FGPM system. The displacements and potentials of cantilever beams combining with sine load, cosine load, step load, and triangular load were analyzed by ISFEM in comparison with FEM.

(1) ISFEM is correct and effective in solving the dynamic response of FGPM structures

(2) ISFEM can reduce the systematic stiffness of FEM and provides calculations closer to the true values

(3) ISFEM is more efficient than FEM and takes less computation time at the same accuracy

This study indicates a possibility to select suitable grading controlled by the power law index according to the application.

Data Availability

The data used to support the findings of this study are included within the article.

Conflicts of Interest

The authors declare no conflicts of interest.

Authors' Contributions

Liming Zhou and Bin Cai performed the simulations. Bin Cai contributed to the writing of the manuscript.

Acknowledgments

Special thanks are due to Professor Guirong Liu for the S-FEM Source Code in http://www.ase.uc.edu/~liugr/software.html. This work was financially supported by the National Key R&D Program of China (grant no. 2018YFF01012401-06), Jilin Provincial Department of Science and Technology Fund Project (grant no. 20170101043JC), Jilin Provincial Department of Education (grant nos. JJKH20180084KJ and JJKH20170788KJ), Fundamental Research Funds for the Central Universities, Science and Technological Planning Project of Ministry of Housing and Urban–Rural Development of the People's Republic of China (2017-K9-047) and Graduate Innovation Fund of Jilin University (grant no. 101832018C184).

References

[1] K. M. Liew, X. Q. He, and S. Kitipornchai, "Finite element method for the feedback control of FGM shells in the frequency domain via piezoelectric sensors and actuators," *Computer Methods in Applied Mechanics and Engineering*, vol. 193, no. 3–5, pp. 257–273, 2004.

[2] G. Song, V. Sethi, and H.-N. Li, "Vibration control of civil structures using piezoceramic smart materials: a review," *Engineering Structures*, vol. 28, no. 11, pp. 1513–1524, 2006.

[3] B. Legrand, J.-P. Salvetat, B. Walter, M. Faucher, D. Théron, and J.-P. Aimé, "Multi-MHz micro-electro-mechanical sensors for atomic force microscopy," *Ultramicroscopy*, vol. 175, pp. 46–57, 2017.

[4] F. Pablo, I. Bruant, and O. Polit, "Use of classical plate finite elements for the analysis of electroactive composite plates.

Numerical validations," *Journal of Intelligent Material Systems and Structures*, vol. 20, no. 15, pp. 1861–1873, 2009.

[5] M. D'Ottavio and O. Polit, "Sensitivity analysis of thickness assumptions for piezoelectric plate models," *Journal of Intelligent Material Systems and Structures*, vol. 20, no. 15, pp. 1815–1834, 2009.

[6] P. Vidal, M. D'Ottavio, M. Ben Thaïer, and O. Polit, "An efficient finite shell element for the static response of piezoelectric laminates," *Journal of Intelligent Material Systems and Structures*, vol. 22, no. 7, pp. 671–690, 2011.

[7] S. B. Beheshti-Aval, M. Lezgy-Nazargah, P. Vidal, and O. Polit, "A refined sinus finite element model for the analysis of piezoelectric-laminated beams," *Journal of Intelligent Material Systems and Structures*, vol. 22, no. 3, pp. 203–219, 2011.

[8] X.-H. Wu, C. Chen, Y.-P. Shen, and X.-G. Tian, "A high order theory for functionally graded piezoelectric shells," *International Journal of Solids and Structures*, vol. 39, no. 20, pp. 5325–5344, 2002.

[9] X. H. Zhu and Z. Y. Meng, "Operational principle, fabrication and displacement characteristic of a functionally gradient piezoelectric ceramic actuator," *Sensors and Actuators A. Physical*, vol. 48, no. 3, pp. 169–176, 1995.

[10] C. C. M. Wu, M. Kahn, and W. Moy, "Piezoelectric ceramics with functional gradients: a new application in material design," *Journal of the American Ceramic Society*, vol. 79, no. 3, pp. 809–812, 2005.

[11] K. Takagi, J.-F. Li, S. Yokoyama, R. Watanabe, A. Almajid, and M. Taya, "Design and fabrication of functionally graded PZT/Pt piezoelectric bimorph actuator," *Science and Technology of Advanced Materials*, vol. 3, no. 2, pp. 217–224, 2002.

[12] G. R. Liu and J. Tani, "Surface waves in functionally gradient piezoelectric plates," *Journal of Vibration and Acoustics*, vol. 116, no. 4, pp. 440–448, 1994.

[13] Z. Zhong and E. T. Shang, "Three-dimensional exact analysis of a simply supported functionally gradient piezoelectric plate," *International Journal of Solids and Structures*, vol. 40, no. 20, pp. 5335–5352, 2003.

[14] C. Piotr, "Three-dimensional natural vibration analysis and energy considerations for a piezoelectric rectangular plate," *Journal of Sound and Vibration*, vol. 283, no. 3–5, pp. 1093–1113, 2005.

[15] W. Q. Chen and H. J. Ding, "On free vibration of a functionally graded piezoelectric rectangular plate," *Acta Mechanica*, vol. 153, no. 3-4, pp. 207–216, 2002.

[16] R. K. Bhangale and N. Ganesan, "Static analysis of simply supported functionally graded and layered magneto-electro-elastic plates," *International Journal of Solids and Structures*, vol. 43, no. 10, pp. 3230–3253, 2006.

[17] M. Lezgy-Nazargah, P. Vidal, and O. Polit, "An efficient finite element model for static and dynamic analyses of functionally graded piezoelectric beams," *Composite Structures*, vol. 104, pp. 71–84, 2013.

[18] M. Lezgy-Nazargah, "A three-dimensional exact state-space solution for cylindrical bending of continuously non-homogenous piezoelectric laminated plates with arbitrary gradient composition," *Archive of Mechanics*, vol. 67, pp. 25–51, 2015.

[19] M. Lezgy-Nazargah, "A three-dimensional Peano series solution for the vibration of functionally graded piezoelectric laminates in cylindrical bending," *Scientia Iranica*, vol. 23, no. 3, pp. 788–801, 2016.

[20] H.-J. Lee, "Layerwise laminate analysis of functionally graded piezoelectric bimorph beams," *Journal of Intelligent Material Systems and Structures*, vol. 16, no. 4, pp. 365–371, 2005.

[21] Z.-C. Qiu, X.-M. Zhang, H.-X. Wu, and H.-H. Zhang, "Optimal placement and active vibration control for piezoelectric smart flexible cantilever plate," *Journal of Sound and Vibration*, vol. 301, no. 3–5, pp. 521–543, 2007.

[22] J. Yang and H. J. Xiang, "Thermo-electro-mechanical characteristics of functionally graded piezoelectric actuators," *Smart Materials and Structures*, vol. 16, no. 3, pp. 784–797, 2007.

[23] B. Behjat, M. Salehi, A. Armin, M. Sadighi, and M. Abbasi, "Static and dynamic analysis of functionally graded piezoelectric plates under mechanical and electrical loading," *Scientia Iranica*, vol. 18, no. 4, pp. 986–994, 2011.

[24] A. Doroushi, M. R. Eslami, and A. Komeili, "Vibration analysis and transient response of an FGPM beam under thermo-electro-mechanical loads using higher-order shear deformation theory," *Journal of Intelligent Material Systems and Structures*, vol. 22, no. 3, pp. 231–243, 2011.

[25] G. W. Wei, Y. B. Zhao, and Y. Xiang, "A novel approach for the analysis of high-frequency vibrations," *Journal of Sound and Vibration*, vol. 257, no. 2, pp. 207–246, 2002.

[26] P. Kudela, M. Krawczuk, and W. Ostachowicz, "Wave propagation modelling in 1D structures using spectral finite elements," *Journal of Sound and Vibration*, vol. 300, no. 1-2, pp. 88–100, 2007.

[27] Y. Kim, S. Ha, and F.-K. Chang, "Time-domain spectral element method for built-in piezoelectric-actuator-induced lamb wave propagation analysis," *AIAA Journal*, vol. 46, no. 3, pp. 591–600, 2008.

[28] H. Zhong and Z. Yue, "Analysis of thin plates by the weak form quadrature element method," *Science China Physics, Mechanics and Astronomy*, vol. 55, no. 5, pp. 861–871, 2012.

[29] X. Wang, Z. Yuan, and C. Jin, "Weak form quadrature element method and its applications in science and engineering: a state-of-the-art review," *Applied Mechanics Reviews*, vol. 69, no. 3, Article ID 030801, 2017.

[30] G. R. Liu and T. Nguyen-Thoi, *Smoothed Finite Element Methods*, CRC Press, Taylor and Francis Group, Boca Raton, FL, USA, 2010.

[31] J.-S. Chen, C.-T. Wu, S. Yoon, and Y. You, "A stabilized conforming nodal integration for Galerkin mesh-free methods," *International Journal for Numerical Methods in Engineering*, vol. 50, no. 2, pp. 435–466, 2001.

[32] K. Y. Dai and G. R. Liu, "Free and forced vibration analysis using the smoothed finite element method (SFEM)," *Journal of Sound and Vibration*, vol. 301, no. 3–5, pp. 803–820, 2007.

[33] S. P. A. Bordas and S. Natarajan, "On the approximation in the smoothed finite element method (SFEM)," *International Journal for Numerical Methods in Engineering*, vol. 81, no. 5, pp. 660–670, 2010.

[34] C. V. Le, H. Nguyen-Xuan, H. Askes, S. P. A. Bordas, T. Rabczuk, and H. Nguyen-Vinh, "A cell-based smoothed finite element method for kinematic limit analysis," *International Journal for Numerical Methods in Engineering*, vol. 83, no. 12, pp. 1651–1674, 2010.

[35] G. R. Liu, W. Zeng, and H. Nguyen-Xuan, "Generalized stochastic cell-based smoothed finite element method (GS_CS-FEM) for solid mechanics," *Finite Elements in Analysis and Design*, vol. 63, pp. 51–61, 2013.

[36] K. Nguyen-Quang, H. Dang-Trung, V. Ho-Huu, H. Luong-Van, and T. Nguyen-Thoi, "Analysis and control of FGM plates integrated with piezoelectric sensors and actuators

using cell-based smoothed discrete shear gap method (CS-DSG3)," *Composite Structures*, vol. 165, pp. 115–129, 2017.

[37] Y. H. Bie, X. Y. Cui, and Z. C. Li, "A coupling approach of state-based peridynamics with node-based smoothed finite element method," *Computer Methods in Applied Mechanics and Engineering*, vol. 331, pp. 675–700, 2018.

[38] G. Liu, M. Chen, and M. Li, "Lower bound of vibration modes using the node-based smoothed finite element method (NS-FEM)," *International Journal of Computational Methods*, vol. 14, no. 4, Article ID 1750036, 2016.

[39] Z. C. He, G. Y. Li, Z. H. Zhong et al., "An ES-FEM for accurate analysis of 3D mid-frequency acoustics using tetrahedron mesh," *Computers & Structures*, vol. 106-107, pp. 125–134, 2012.

[40] X. Y. Cui, G. Wang, and G. Y. Li, "A nodal integration axisymmetric thin shell model using linear interpolation," *Applied Mathematical Modelling*, vol. 40, no. 4, pp. 2720–2742, 2016.

[41] X. Y. Cui, X. B. Hu, and Y. Zeng, "A copula-based perturbation stochastic method for fiber-reinforced composite structures with correlations," *Computer Methods in Applied Mechanics and Engineering*, vol. 322, pp. 351–372, 2017.

[42] T. Nguyen-Thoi, G. R. Liu, K. Y. Lam, and G. Y. Zhang, "A face-based smoothed finite element method (FS-FEM) for 3D linear and geometrically non-linear solid mechanics problems using 4-node tetrahedral elements," *International Journal for Numerical Methods in Engineering*, vol. 78, no. 3, pp. 324–353, 2009.

[43] Z. C. He, G. Y. Li, Z. H. Zhong et al., "An edge-based smoothed tetrahedron finite element method (ES-T-FEM) for 3D static and dynamic problems," *Computational Mechanics*, vol. 52, no. 1, pp. 221–236, 2013.

[44] E. Li, Z. C. He, X. Xu, and G. R. Liu, "Hybrid smoothed finite element method for acoustic problems," *Computer Methods in Applied Mechanics and Engineering*, vol. 283, pp. 664–688, 2015.

[45] C. Jiang, Z.-Q. Zhang, G. R. Liu, X. Han, and W. Zeng, "An edge-based/node-based selective smoothed finite element method using tetrahedrons for cardiovascular tissues," *Engineering Analysis with Boundary Elements*, vol. 59, pp. 62–77, 2015.

[46] X. B. Hu, X. Y. Cui, Z. M. Liang, and G. Y. Li, "The performance prediction and optimization of the fiber-reinforced composite structure with uncertain parameters," *Composite Structures*, vol. 164, pp. 207–218, 2017.

[47] X. Cui, S. Li, H. Feng, and G. Li, "A triangular prism solid and shell interactive mapping element for electromagnetic sheet metal forming process," *Journal of Computational Physics*, vol. 336, pp. 192–211, 2017.

[48] G. R. Liu, H. Nguyen-Xuan, and T. Nguyen-Thoi, "A theoretical study on the smoothed FEM (S-FEM) models: properties, accuracy and convergence rates," *International Journal for Numerical Methods in Engineering*, vol. 84, no. 10, pp. 1222–1256, 2010.

[49] E. Li, Z. C. He, G. Wang, and G. R. Liu, "An efficient algorithm to analyze wave propagation in fluid/solid and solid/fluid phononic crystals," *Computer Methods in Applied Mechanics and Engineering*, vol. 333, pp. 421–442, 2018.

[50] W. Zeng, G. R. Liu, D. Li, and X. W. Dong, "A smoothing technique based beta finite element method (βFEM) for crystal plasticity modeling," *Computers & Structures*, vol. 162, pp. 48–67, 2016.

[51] H. Nguyen-Xuan, G. R. Liu, T. Nguyen-Thoi, and C. Nguyen-Tran, "An edge-based smoothed finite element method for analysis of two-dimensional piezoelectric structures," *Smart Materials and Structures*, vol. 18, no. 6, Article ID 065015, 2009.

[52] H. Nguyen-Van, N. Mai-Duy, and T. Tran-Cong, "A smoothed four-node piezoelectric element for analysis of two-dimensional smart structures," *Computer Modeling in Engineering and Sciences*, vol. 23, no. 3, pp. 209–222, 2008.

[53] P. Phung-Van, T. Nguyen-Thoi, T. Le-Dinh, and H. Nguyen-Xuan, "Static and free vibration analyses and dynamic control of composite plates integrated with piezoelectric sensors and actuators by the cell-based smoothed discrete shear gap method (CS-FEM-DSG3)," *Smart Materials and Structures*, vol. 22, no. 9, Article ID 095026, 2013.

[54] Z. C. He, E. Li, G. R. Liu, G. Y. Li, and A. G. Cheng, "A mass-redistributed finite element method (MR-FEM) for acoustic problems using triangular mesh," *Journal of Computational Physics*, vol. 323, pp. 149–170, 2016.

[55] W. Zuo and K. Saitou, "Multi-material topology optimization using ordered SIMP interpolation," *Structural and Multidisciplinary Optimization*, vol. 55, no. 2, pp. 477–491, 2017.

[56] E. Li, Z. C. He, J. Y. Hu, and X. Y. Long, "Volumetric locking issue with uncertainty in the design of locally resonant acoustic metamaterials," *Computer Methods in Applied Mechanics and Engineering*, vol. 324, pp. 128–148, 2017.

[57] L. Chen, Y. W. Zhang, G. R. Liu, H. Nguyen-Xuan, and Z. Q. Zhang, "A stabilized finite element method for certified solution with bounds in static and frequency analyses of piezoelectric structures," *Computer Methods in Applied Mechanics and Engineering*, vol. 241–244, pp. 65–81, 2012.

[58] L. Zhou, M. Li, Z. Ma et al., "Steady-state characteristics of the coupled magneto-electro-thermo-elastic multi-physical system based on cell-based smoothed finite element method," *Composite Structures*, vol. 219, pp. 111–128, 2019.

[59] L. Zhou, S. Ren, G. Meng, X. Li, and F. Cheng, "A multi-physics node-based smoothed radial point interpolation method for transient responses of magneto-electro-elastic structures," *Engineering Analysis with Boundary Elements*, vol. 101, pp. 371–384, 2019.

[60] H. Nguyen-Van, N. Mai-Duy, and T. Tran-Cong, "A node-based element for analysis of planar piezoelectric structures," *CMES: Computer Modeling in Engineering & Sciences*, vol. 36, no. 1, pp. 65–96, 2008.

[61] E. Li, Z. C. He, Y. Jiang, and B. Li, "3D mass-redistributed finite element method in structural-acoustic interaction problems," *Acta Mechanica*, vol. 227, no. 3, pp. 857–879, 2016.

[62] L. Zhou, M. Li, G. Meng, and H. Zhao, "An effective cell-based smoothed finite element model for the transient responses of magneto-electro-elastic structures," *Journal of Intelligent Material Systems and Structures*, vol. 29, no. 14, pp. 3006–3022, 2018.

[63] L. Zhou, M. Li, H. Zhao, and W. Tian, "Cell-based smoothed finite element method for the intensity factors of piezoelectric bimaterials with interfacial crack," *International Journal of Computational Methods*, vol. 16, no. 7, Article ID 1850107, 2019.

[64] J. Zheng, Z. Duan, and L. Zhou, "A coupling electromechanical cell-based smoothed finite element method based on micromechanics for dynamic characteristics of piezoelectric composite materials," *Advances in Materials Science and Engineering*, vol. 2019, Article ID 4913784, 16 pages, 2019.

[65] L. Zhou, S. Ren, C. Liu, and Z. Ma, "A valid inhomogeneous cell-based smoothed finite element model for the transient

characteristics of functionally graded magneto-electro-elastic structures," *Composite Structures*, vol. 208, pp. 298–313, 2019.

[66] L. Zhou, M. Li, B. Chen, F. Li, and X. Li, "An inhomogeneous cell-based smoothed finite element method for the nonlinear transient response of functionally graded magneto-electro-elastic structures with damping factors," *Journal of Intelligent Material Systems and Structures*, vol. 30, no. 3, pp. 416–437, 2019.

[67] R. X. Yao and Z. F. Shi, "Steady-state forced vibration of functionally graded piezoelectric beams," *Journal of Intelligent Material Systems and Structures*, vol. 22, no. 8, pp. 769–779, 2011.